

Geomechanics and Geoengineering



An International Journal

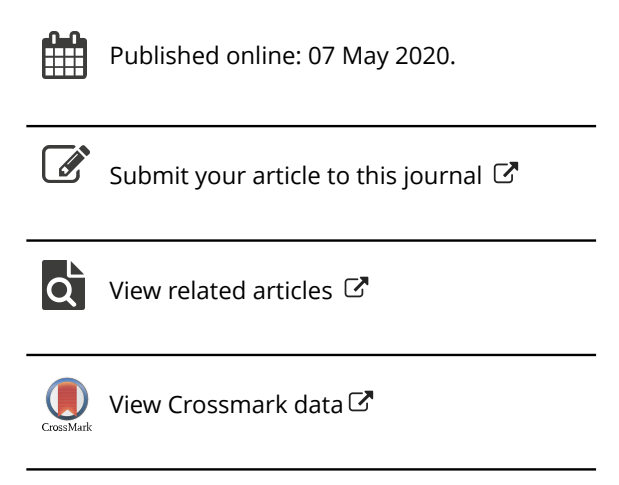
ISSN: 1748-6025 (Print) 1748-6033 (Online) Journal homepage: https://www.tandfonline.com/loi/tgeo20

Explanations of anisotropic strength and fabric evolution in granular soils by DEM simulations and buckling failure theory

Junxing Zheng, Hantao He & Zhaochao Li

To cite this article: Junxing Zheng, Hantao He & Zhaochao Li (2020): Explanations of anisotropic strength and fabric evolution in granular soils by DEM simulations and buckling failure theory, Geomechanics and Geoengineering, DOI: 10.1080/17486025.2020.1755465

To link to this article: https://doi.org/10.1080/17486025.2020.1755465







Explanations of anisotropic strength and fabric evolution in granular soils by DEM simulations and buckling failure theory

Junxing Zheng (Da, Hantao He (Db) and Zhaochao Li (Dc)

^aDepartment of Civil, Construction and Environmental Engineering, Iowa State University, Ames, IA, USA; ^bGraduate Student Research Assistant, Department of Civil, Construction and Environmental Engineering, Iowa State University, Ames, IA, USA; ^cAssistant Professor, Department of Engineering and Technology Management, Morehead State University, Morehead, KY, USA

ABSTRACT

This research aims to discover a micro explanation of anisotropic strength of granular soils caused by different inherent fabrics based on the discrete element method (DEM) simulations. Soil particles are simulated as ellipsoids (i.e., clumped spheres) to preserve the elongation distributions of real soil particles that are determined by analysing 90,000 particles from 18 sands. Then, virtual soil specimens are prepared at 12 different inherent fabrics by restricting the particle long axis orientations. For each inherent fabric, triaxial tests are simulated at five intermediate stress ratio values, resulting in a total of 60 DEM simulations. The relationships between anisotropic shear strength and fabric evolution are investigated based on simulation results. For a specific inherent fabric, Lade's isotropic failure theory can be used to describe shear strengths and octahedral contact normal fabric factors at peak and critical states. A buckling failure theory from structural engineering is introduced to explain the anisotropic strength of granular soils and fabric evaluations observed in laboratory tests and simulations. As the angle between loading and fabric direction increases from zero to 90 degrees, the conceptual widths of soil columns decrease, leading to the smaller buckling failure loads and therefore the smaller shear strength of granular soils.

ARTICLE HISTORY

Received 13 December 2019 Accepted 9 April 2020

KEYWORDS

Inherent and induced fabric; fabric anisotropy; discrete element method; granular soils; buckling failure theory

1. Introduction

In natural sedimentary soils, particles depositing through water and air generally align their largest projected surface normal to the depositional direction. Therefore, cross-anisotropic fabric develops in alluvial, coastal, and lacustrine deposits (Zheng and Hryciw 2017, 2018). The cross-anisotropic structure of granular soils features their inhomogeneous shear strength.

If the deposit direction is defined as fabric direction (f), laboratory tests have illustrated that the macromechanical behaviour of granular soils depends on the relative angles (θ) between f and loading direction as shown in Figure 1(a). For example, in Figure 1(b), anisotropic shear strengths of sands have been observed in triaxial tests on various sands including Cambria sand (Ochiai and Lade 1983), Leighton Buzzard sand (Arthur and Menzies 1972), Ham river sand (Arthur and Phillips 1975), and Toyoura sand (Oda 1972a). In these triaxial tests, soil specimens were prepared at different θ values from 0° to 90°. As θ increases from 0° to 90°, the peak friction angle ϕ_p decreases about 2°. The influences of fabric anisotropy on strength of sands have also been observed by other researchers (Oda

1972b, 1981, Arthur et al. 1977, Oda et al. 1978, 1998, Wong and Arthur 1985, Tatsuoka et al. 1986b, 1986a; Lam W-K and Tatsuoka 1988; Lade et al. 2015, Yang et al. 2016).

The anisotropic shear strength of granular soils observed in Figure 1 affects the bearing capacity of granular soils. The laboratory test results showed that when θ values increased from 0° to 90°, bearing capacity typically decreased by 25%-34% (Azami *et al.* 2009). Such a large variance may profoundly affect the stability of foundations, and therefore, the safety of structures.

The soil fabric is commonly quantified by scalar parameters, including coordination number and void ratio, and directional parameters such as particle long axes and contact normals (Sun et al. 2019, Sun and Zheng 2019). These micro particle-level parameters are difficult to measure in laboratory tests. As such, the discrete element method (DEM) has become a predominant tool to investigate fabric evaluations of granular soils. Many researchers have conducted DEM simulations to explore the relationships between fabric and macro mechanical behaviour of granular soils (Cui et al. 2007, O'sullivan et al.'s 2008, Wang and Gutierrez

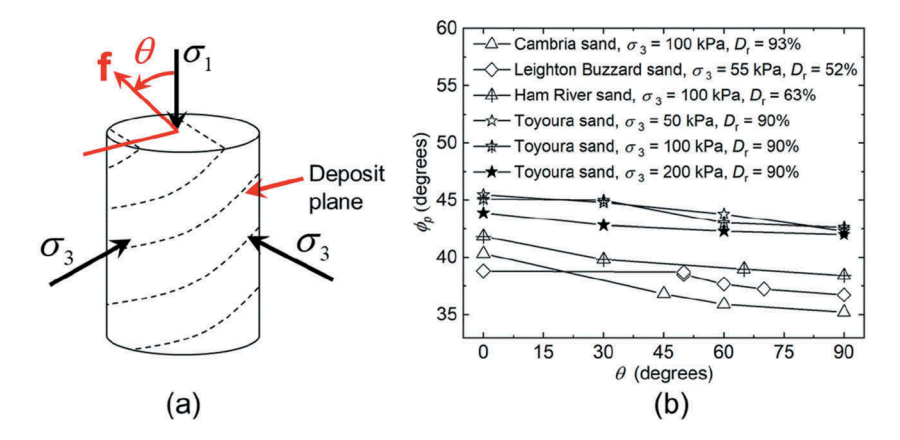


Figure 1. The anisotropic strength of different sands caused by different inherent fabrics.

2010, Yimsiri and Soga 2010, Guo and Zhao 2013, Huang *et al.* 2014, Zhao and Guo 2015).

This paper aims to investigate the origin of anisotropic strength observed in laboratory tests in Figure 1(b) based on DEM simulations. Soil particles are idealised as ellipsoids to preserve the elongation distributions of real soil particles. Then, virtual soil specimens are prepared at different inherent fabrics including four fabric directions of $\theta = 0^{\circ}$, 30°, 60°, and 90° and three fabric degrees of strong, medium, and weak fabrics by restricting the particle long axis orientations. Therefore, 12 inherent fabrics are generated. The triaxial tests are simulated at five intermediate stress ratio values with $b = (\sigma_2 - \sigma_3)/(\sigma_1)$ $-\sigma_3$) values of 0, 0.25, 0.5, 0.75, and 1.0. Therefore, a total of 60 DEM simulations are performed. Based on simulation results, this study explores the induced fabric anisotropy in triaxial tests and develops a micro explanation of anisotropic strength of granular soils caused by different inherent and induced fabrics.

2. Stress and fabric tensor

The homogenised bulk stress tensor for a discrete particle assembly can be calculated from the Love formula (Christoffersen *et al.* 1981):

$$\sigma_{ij} = \frac{1}{V} \sum_{c=1}^{N_c} f_i d_j \tag{1}$$

where V is the volume of the assembly, N_c is the total number of contacts, f is the contact force, and d is a vector connecting the centres of two contacting particles. The mean effective stress is $p' = \sigma_{ii}/3$ and the equivalent deviatoric stress can be determined as:

$$q_e = \frac{1}{\sqrt{2}} \left[(\sigma_1 - \sigma_2)^2 + (\sigma_1 - \sigma_3)^2 + (\sigma_2 - \sigma_3)^2 \right]^{0.5}$$
(2)

where q_e becomes the traditional definition of the deviatoric stress $q = \sigma_1 - \sigma_3$ for triaxial tests.

This study used particle long axes and contact normals to quantify fabric and investigate inherent and induced fabrics in simulations. Therefore, fabric tensor can be defined as:

$$\varphi_{ij}^* = \int_{\Omega} E(\Omega) n_i^* n_j^* d\Omega \ (* = p, c)$$
 (3)

where the superscript * represents either 'p' or 'c' meaning particle long axis tensor or contact normal tensor in the rest of the paper; n_i^* (i=1,2,3) is the components of a unit vector n^* which could be either particle long axis (* = p) or contact normal (* = c); and $E(\Omega)$ is a density function describing the statistical distribution of n^* ; and Ω is a solid angle corresponding to the entire surface of a unit sphere. The $E(\Omega)$ can be approximated by the second-order Fourier expansion (Kanatani 1984, Ouadfel and Rothenburg 2001):

$$E(\Omega) = \frac{1}{4\pi} \left(1 + F_{ij}^* n_i^* n_j^* \right) (* = p, c)$$
 (4)

where F_{ij}^* is the deviatoric fabric tensor:

$$F_{ij}^* = \frac{15}{2} \left(\varphi_{ij}^* - \frac{1}{5} \delta_{ij} \right) (* = p, c)$$
 (5)

where δ_{ij} is the Kronecker delta.

For the assembly of discrete particles, the Eq. (3) can be rewritten as a limited form:

$$\varphi_{ij}^* = \frac{1}{N^*} \sum_{N^*} n_i^* n_j^* (* = p, c)$$
 (6)

where N^* is the total number of vectors n^* in assembly. The Eq. (6) has been widely used in DEM studies to compute fabric tensor.

The spatial distribution of vectors n^* (* = p, c) is commonly plotted as a 3D rose diagram as shown in

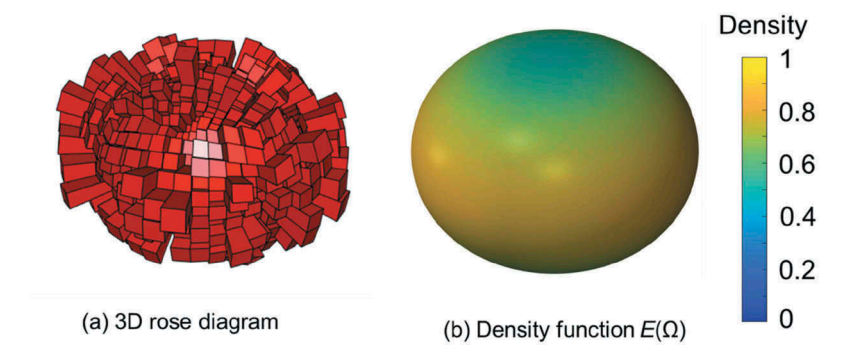


Figure 2. Illustration of density function $E(\Omega)$.

Figure 2(a). Given spatial distribution of n^* (* = p, c), Eqs. (4), (5), and (6) can be used to determine the $E(\Omega)$. The $E(\Omega)$ is plotted in Figure 2(b), which is essentially a best surface to the 3D rose diagram in Figure 2(a). The $E(\Omega)$ diagram provides an easier way to observe the preferred fabric direction and degree of fabric anisotropy than the 3D rose diagram.

To measure the degree of fabric anisotropy under three-dimensional stress condition, Barreto and O'Sullivan (2012) proposed a generalised octahedral fabric factor:

$$\Psi^* = \frac{1}{\sqrt{2}} \left[\left(\varphi_1^* - \varphi_2^* \right)^2 + \left(\varphi_1^* - \varphi_3^* \right)^2 + \left(\varphi_2^* - \varphi_3^* \right)^2 \right]^{0.5} (* = p, c)$$
(7)

where φ_1^* , φ_2^* , and φ_3^* are the principal values of φ_{ij}^* . The Eq. (6) reduces to $\varphi_d^* = \varphi_1^* - \varphi_3^*$ for axisymmetric triaxial test condition (Thornton 2000).

3. Virtual soil specimen generation

The fabric anisotropy of granular soils depends on particle elongations. Laboratory studies have shown that elongated soils tend to develop larger degrees of fabric anisotropy (Oda 1981, Lade et al. 2014, Zheng and Hryciw 2017, 2018). The elongation of soil particle can be quantified by the ratio of width d_2 to length d_1 , which is defined as width to length ratio sphericity (S_{WL}) (Krumbein and Sloss 1951). To investigate the S_{WL} values of natural sands, a total of 18 natural sands are collected and analysed. For each sand, around 5,000 particles are analysed by the computational geometry code (Zheng and Hryciw 2015, Hryciw et al. 2016). The distributions of $S_{\rm WL}$ values are plotted in Figure 3(a). The mean S values $(S_{WL, m})$ are computed and shown in the legend of each sand. For example, the S_{WL, m} of brady, TX is 0.76.

To preserve the particle elongations in simulations, the soil particles are idealised as ellipsoids in DEM. This study generates 14 ellipsoids with $S_{\rm WL}$ values varying

from 0.35 to 1.00 with an increment of 0.05. The DEM simulations were performed using the Particle Flow Code in Three Dimensions (PFC3D) (Itasca Consulting Group 2018). These ellipsoids are simulated as sphere clumps are

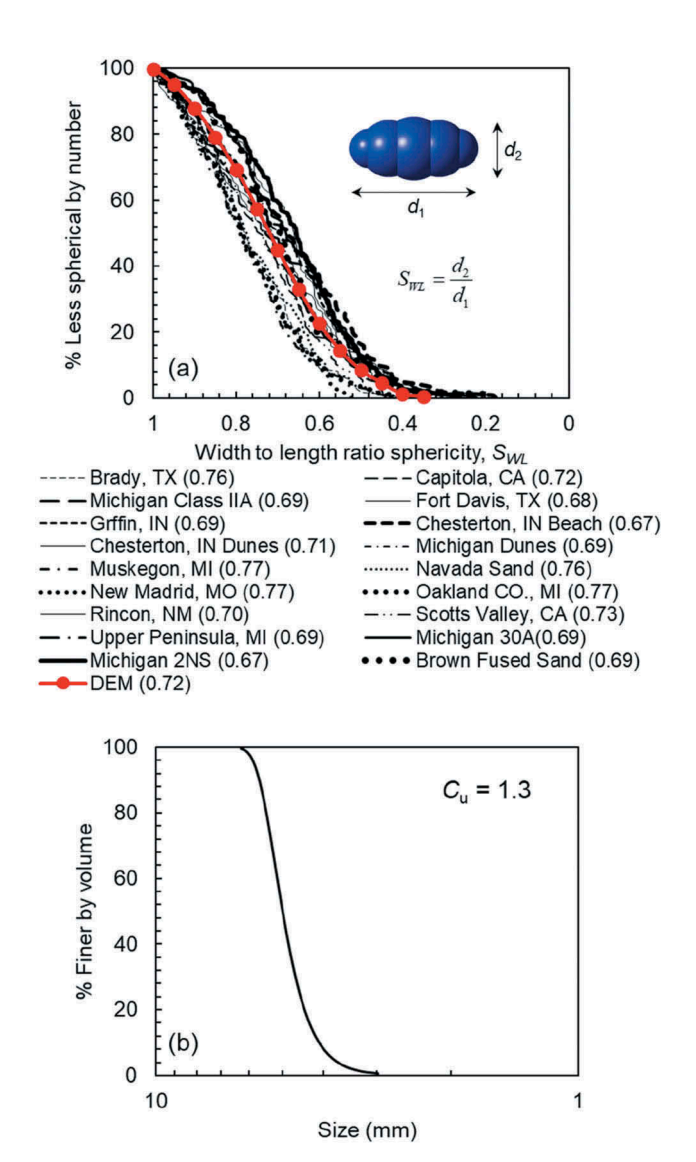


Figure 3. Particle shape and size distributions of virtual soil specimen in DEM consisting of ellipsoids.

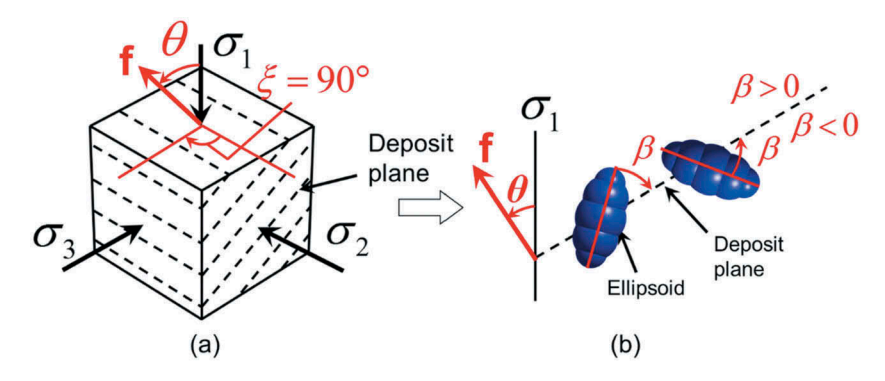


Figure 4. Illustration of inherent cross-anisotropic fabrics in DEM.

shown in Figure 3(a). The virtual specimen contains 10,685 particles with the combination of 14 ellipsoids satisfying the mean $S_{\rm WL}$ distribution of these natural soils. The $S_{\rm WL, m}$ of the virtual soil is 0.72. The particle size is defined as the diameter of volume equivalent sphere of ellipsoid. The sizes of ellipsoids are randomly enlarged and reduced to generate a particle size distribution as shown in Figure 3(b).

As discussed before, the fabric anisotropy of granular soils depends on particle $S_{\rm WL}$. Therefore, the ellipsoids used in DEM with the average $S_{\rm WL}$ distribution may be representative for the $S_{\rm WL}$ distributions of natural sands. Therefore, the fabric evolution simulation results may provide insight into the actual fabric evolution in actual sands. This paper uses ellipsoids in simulations, rather than realistic particles. Therefore, direct comparisons between simulation and laboratory tests are not meaningful. The particle size distribution in Figure 3(b) is used in simulation considering computational capability. If we use large $C_{\rm u}$, the simulation will include a large number of small ellipsoids, exceeding the computational capability of our workstation.

4. Inherent fabrics in virtual soil specimens

The 10,685 ellipsoids are distributed in a 10 cm \times 10 cm \times 10 cm cubic box bounded by rigid walls. The orientations of those ellipsoids are controlled to develop different inherent cross-anisotropic fabrics as shown in Figure 4(a). The direction of inherent cross-anisotropic fabric is quantified by fabric direction (f), which is the normal of the despite plane. The vector f is determined by two spherical coordinates θ and ξ in principal stress space, where θ and ξ are the angles between f and σ_1 and σ_2 , respectively, as shown in Figure 4(a). The degree of inherent fabric is quantified by the octahedral fabric factor (Ψ^* , * = p, c), which is computed by Eq. (7). The Ψ^* depends on relative angle θ between ellipsoids and the deposit plane as shown in Figure 4(b). The θ values of ellipsoids vary from -90° to

90°. If all the θ values of ellipsoids are restricted as 0°, this generates a strong cross-anisotropic fabric. If the θ values of ellipsoids are randomly distributed in [-90°, 90°], this essentially generates an isotropic fabric.

	Ī						
Fabric	Particle fabric			Contact fabric			
Strong fabric	(a) upposition 0.2 0.2 0.2 0.2 0.2 0.3 direction			(b) uo12 02 02 03 direction			
	φ_1^p	φ_2^p	φ_3^p	$arphi_1^c$	φ_2^c	φ_3^c	
	0.40	0.40	0.20	0.37	0.32	0.31	
	Ч	$y^p = 0.2$	o = 0.20		$\Psi^c = 0.05$		
Medium fabric	(C) using of the control of the cont			(d) to the control of			
	$arphi_1^p$	$arphi_2^p$	φ_3^p	$arphi_1^c$	φ_2^c	φ_3^c	
	0.40	0.36	0.24	0.36	0.32	0.32	
	Ψ ^p = 0.15			$\Psi^c = 0.04$			
Weak fabric	(e) up 0.2 0.2 0.2 0.2 0.2 0.2 0.2 0.2 0.2 0.2			(f) 0.2 0.2 0.2 0.2 0.2 0.2 0.2 0.2 0.2 0.2			
	φ_1^p	φ_2^p	φ_3^p	φ_1^c	φ_2^c	φ_3^c	
	0.37	0.36	0.27	0.35	0.34	0.31	
	Ψ ^p = 0.10			$\Psi^c = 0.03$			

Figure 5. Illustration of the inherent fabric for $\theta=30^\circ$ after consolidation.

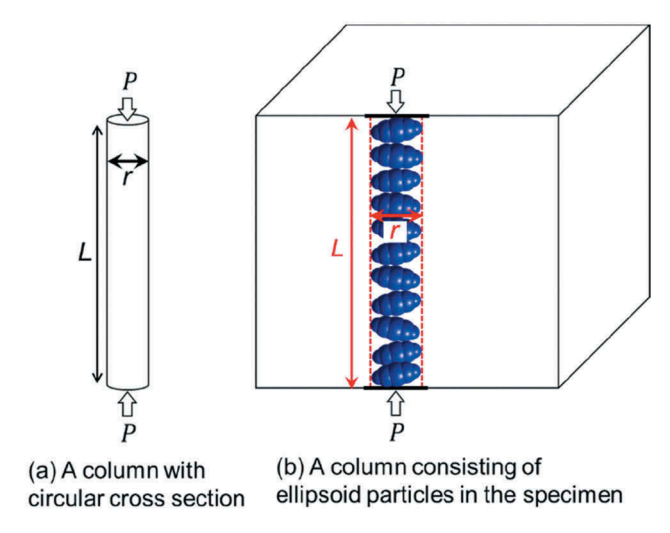


Figure 6. Illustration of column buckling failure theory.

This study simulates four fabric directions: $\theta = 0^\circ$, 30° , 60° , and 90° while ξ keeps 90° . For each direction, three different degrees of fabric anisotropy are simulated by defining the three ranges of θ values: $[0^\circ, 0^\circ]$, $[-45^\circ, 45^\circ]$, and $[-80^\circ, 80^\circ]$, which are defined as strong, medium and weak fabrics, respectively. It should be noted that these strong, medium and weak fabrics are defined for discriminating three initial fabric conditions in our simulations, which are not used for fabric quantification in this study. We use octahedral fabric factor $(\Psi^*, *= p, c)$ for quantifying fabric.

The combinations of fabric directions and fabric degrees generate 12 inherent fabrics. All the specimens are consolidated under the isotropic stress $\sigma_1 = \sigma_2 = \sigma_3 = 500$ kPa. During consolidation, friction coefficient μ is set as zero to reach the dense packing. The linear contact model of PFC is used in simulations. The effective

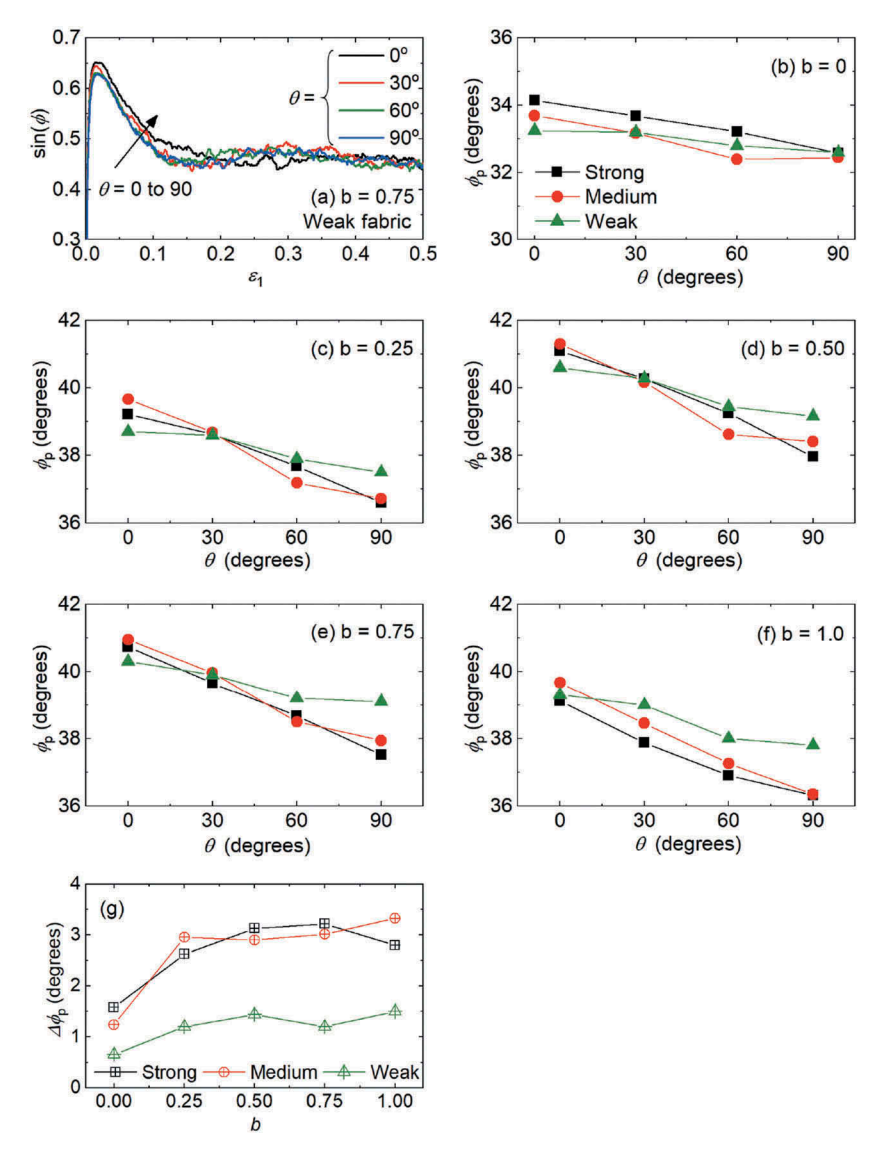


Figure 7. Anisotropic strength of granular soils in simulations as a function of different inherent fabrics and triaxial strain conditions (b).

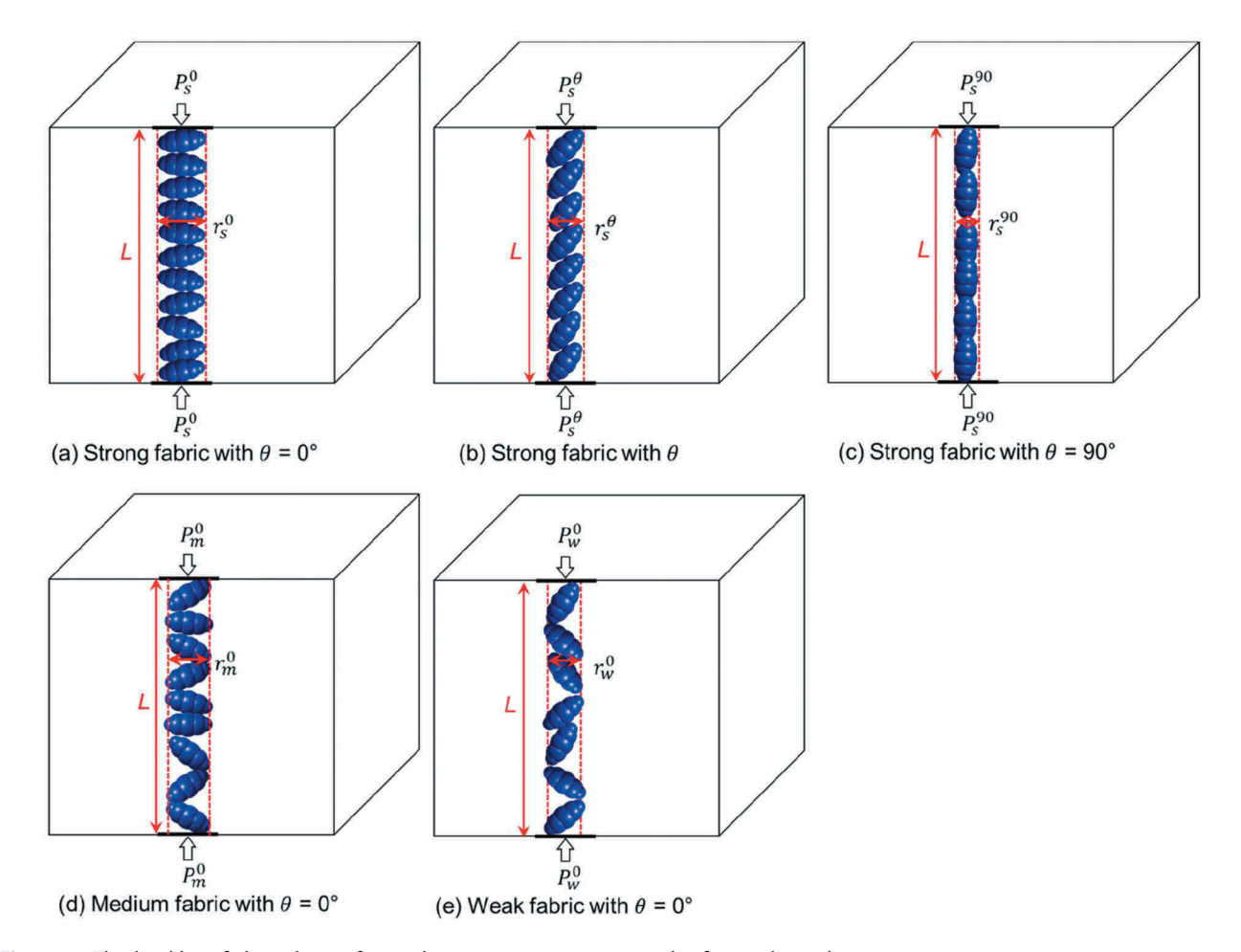


Figure 8. The buckling failure theory for explaining anisotropic strength of granular soils.

modulus E^* of wall is set as 2.5 GPa, while the E^* of ellipsoid is set as 0.25 GPa. The normal-to-shear stiffness ratio κ^* is set as 1.5. Particle rotations are not constrained in consolidation to create interlocking and accommodate the macro deformation under isotropic stresses.

After consolidation, θ values are not changed, indicating the consolidation process does not change fabric direction. The octahedral particle long axis fabric factor Ψ^p values for strong, medium, and weak fabrics are around 0.20, 0.15, and 0.10, respectively, for different fabric directions. The octahedral contact normal fabric factor Ψ^c values for strong, medium, and weak fabrics are around 0.05, 0.04, and 0.03, respectively, for different fabric directions. The spatial distributions of particle long axes and contact normals are quantified by density functions $E(\Omega)$ based on Eqs. (4), (5), and (6). After consolidation, the $E(\Omega)$ plots for particle long axes and contact normals for θ = 30° are shown in Figure 5. The φ_1^* , φ_2^* , φ_3^* , and Ψ^* (* = p, c) values are also superimposed.

After consolidation, particle long axes display a cross-anisotropic fabric. In the deposit plane, φ_1^p values are close to φ_2^p values and both are larger than φ_3^p values.

However, after consolidation, contact normals display an isotropic fabric. The φ_1^c , φ_2^c , and φ_3^c values are close to each other and Ψ^c values are close to zero. That is expected because the same amount of contact normals are mobilised in each direction to establish the force chains in specimen to retain external isotropic stresses.

5. Buckling failure theory

In structural engineering, the critical buckling pressure of a column with circular cross section and pinned at both ends can be quantified by (Li *et al.* 2019a, 2019b, 2019e, 2019c, 2019d):

$$P = \pi^2 E \left(\frac{r}{L}\right)^2 \tag{8}$$

where r is the radius of the column and L is the length column as shown in Figure 6(a).

After consolidation, we cut a vertical column of ellipsoids from the specimen as shown in Figure 6(b). The critical buckling pressure P of this column of ellipsoids can be quantified by Eq. (8) as shown in Figure 6

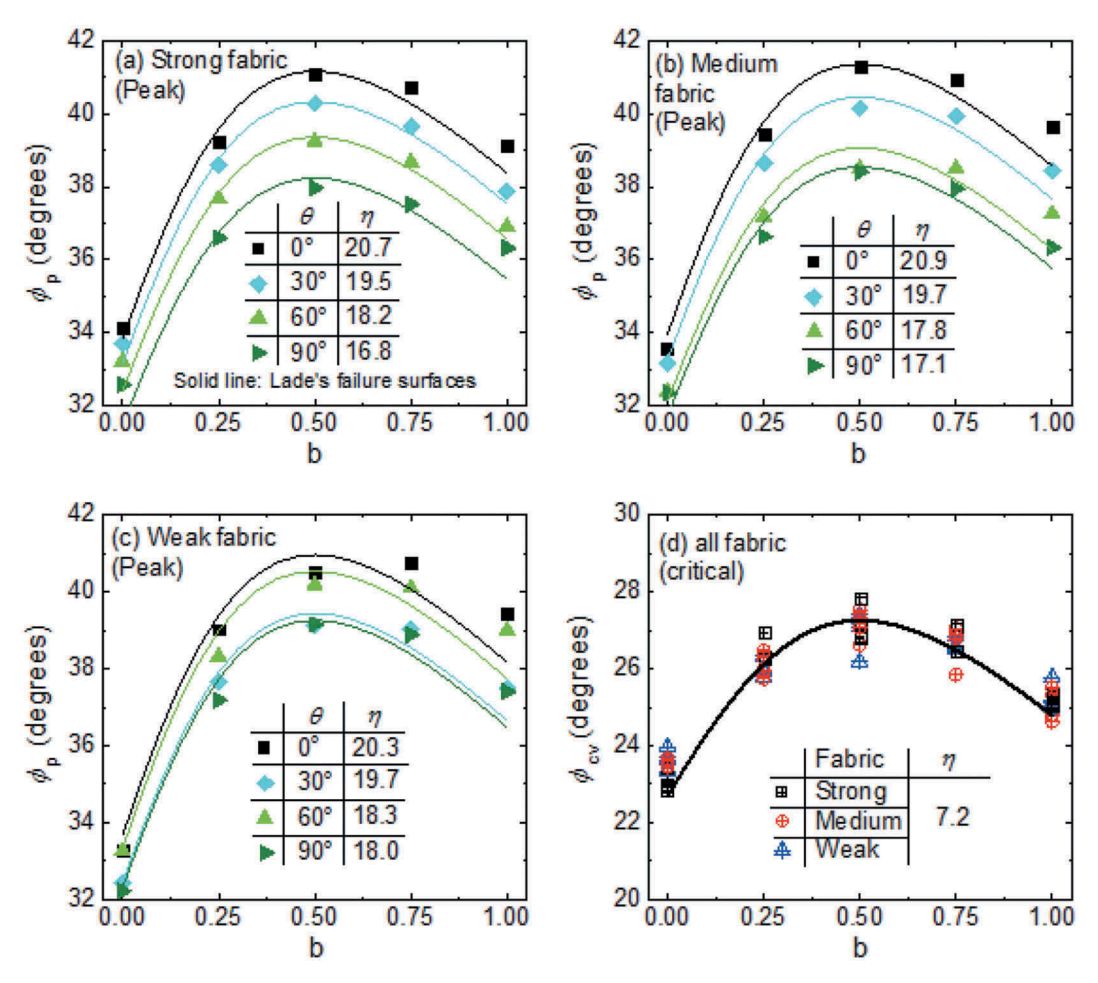


Figure 9. The relationships between peak mobilised friction angles (ϕ_p) , critical mobilised friction angles (ϕ_{cv}) , and triaxial strain conditions (b).

(b). We will use Eq. (8) to analyse the anisotropic strength and fabric evolution in granular soils.

6. Macro-mechanical responses

After consolidation, the soil specimens are sheared under the constant mean effective stress p' = 500 kPa and constant stress ratio $b = (\sigma_2 - \sigma_3)/(\sigma_1 - \sigma_3)$. For each of 12 inherent fabrics, five b values of 0, 0.25, 0.5, 0.75, and 1.0 are used, generating five shear simulations. Therefore, there are total of 60 DEM simulations are performed. The contact friction coefficient μ is set as 0.5 in shear stage.

The mobilised shear strength $\sin(\phi) = (\sigma_1 - \sigma_3)/(\sigma_1 + \sigma_3)$ of different θ values at strong fabric and b = 0.25 are plotted against vertical strain ε_1 in Figure 7(a). The $\sin(\phi)$ increases as increasing ε_1 until reach the peak around $\varepsilon_1 = 0.025$. Then, all the $\sin(\phi)$ curves converge to the same critical state regardless of the different inherent fabrics. The $\sin(\phi)$ versus ε_1 curves of other tests have a similar tendency as Figure 7(a), so they are not displayed.

The peak friction angles ϕ_p of all the simulations are computed and plotted versus θ in Figure 7(b–f). All the ϕ_p values monotonically decrease as θ increases from 0° to 90°. It is interesting to observe that the ϕ_p values of weak fabric are smaller than the ϕ_p values of strong fabric at small θ (θ = 0° and 30°), but opposite trends are observed at large θ (θ = 60° and 90°).

The variation ranges of ϕ_p values ($\Delta\phi_p$) are different depending on the inherent fabric degrees and b values. Therefore, the $\Delta\phi_p$ values are computed and shown in Figure 7(g). The $\Delta\phi_p$ values for strong and medium fabrics are close and both are larger than $\Delta\phi_p$ for weak fabric. The $\Delta\phi_p$ increases as b increases.

The buckling failure theory of Eq. (8) is used to explain the anisotropic strength observed in Figure 7(b) to (f). For example, three cubic specimens with strong fabric with different θ values are shown in Figure 8(a–c). The vertical columns of ellipsoids are cut from three specimens. The specimens have the same height, but radii of columns vary contingent on inherent fabric directions, which is defined as r_s^0 , r_s^0 , and r_s^{90} , respectively. With increasing θ values, the

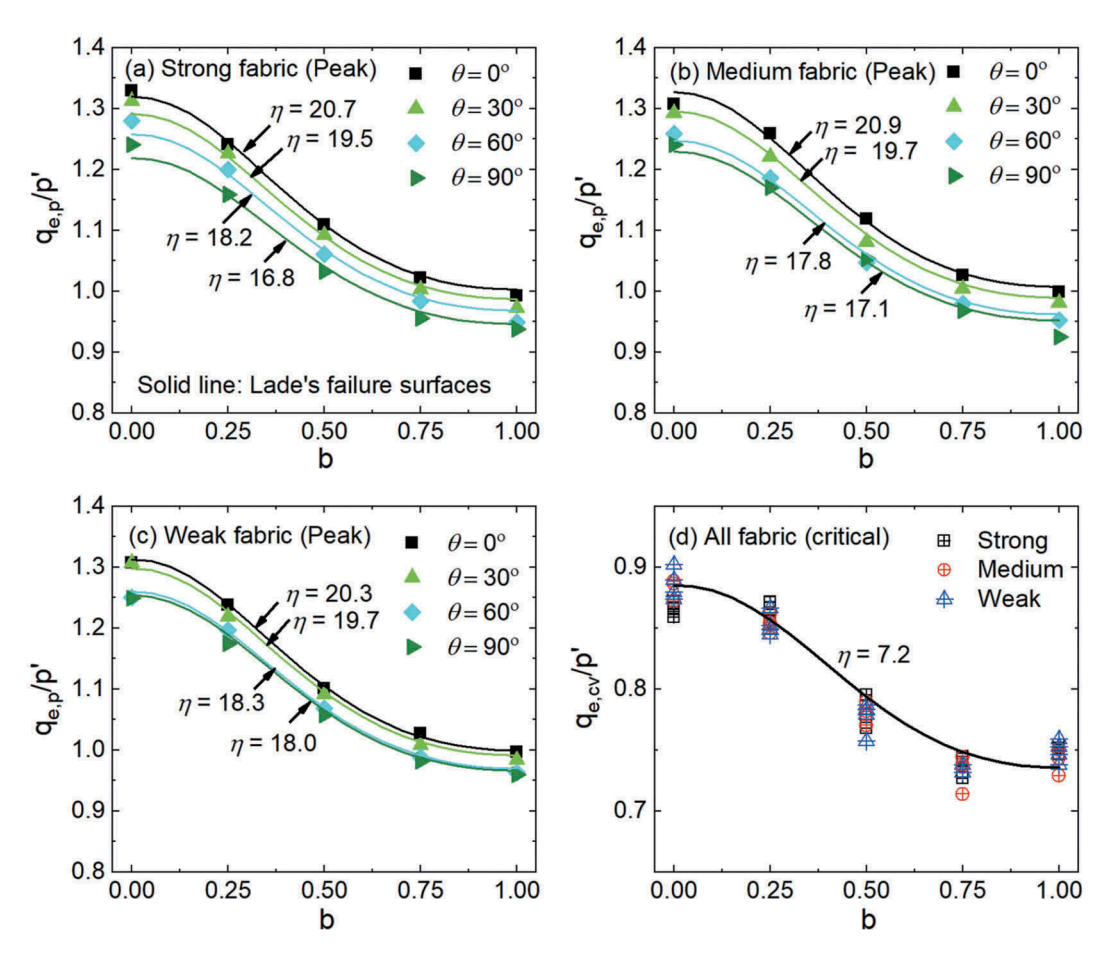


Figure 10. The relationships between peak mobilised stress ratios ($q_{e,p}/p'$), mobilised stress ratios at critical state ($q_{e,cv}/p'$), and triaxial strain conditions (b).

r decreases: $r_s^0 > r_s^0 > r_s^{90}$. Therefore, based on Eq. (8), the critical buckling pressure of a column P also decreases: P_s^0 > $P_s^{\theta} > P_s^{90}$. The critical buckling pressure P determines the peak friction angle ϕ_p values of the specimen, so ϕ_p decrease along with increasing θ values. This explains the decreasing $\phi_{\rm p}$ values of strong fabric in Figure 7.

The same concept can also be used to explain the decreasing ϕ_p values of the specimens with medium and weak fabrics. We can also cut vertical columns of ellipsoids from specimens with medium and weak fabrics but $\theta = 0^{\circ}$ as shown in Figure 8(d-e). As degrees of fabric anisotropy become weaker, the r decreases: $r_s^0 >$ $r_m^0 > r_w^0$ as shown in Figure 8(a), (d) and (e). Therefore, the ϕ_p values decrease when degrees of fabric anisotropy change from strong fabric to weak fabric.

The ϕ_p values are plotted against b values in Figure 9(a–c). The $\phi_{\rm p}$ values of the same θ follows a bell shape as b increases from 0 to 1. The maximum ϕ_p occurs at b = 0.5 while the minimum $\phi_{\rm p}$ occurs at b = 0. The critical friction angles $\phi_{\rm cv}$ are computed by averaging the ϕ values in a range of $\varepsilon_1 = 0.4$ to 0.5. All the ϕ_{cv} values are plotted in Figure 9(d). For the same b condition, all the ϕ_{cv} values collapse together,

indicating ϕ_{cv} values are independent of inherent fabrics. However, for different b conditions, the ϕ_{cv} values exhibit the same trend with $\phi_{\rm p}$ values, following a bell shape as b increases from 0 to 1. The similar observation has been made by other researchers (Ng 2004, Huang et al. 2014).

Lade (Lade 1977) proposed a two-parameter failure criterion for cohesionless soils based on observations of laboratory tests:

$$\left(\frac{I_1^3}{I_3} - 27\right) \left(\frac{I_1}{p_a}\right)^m = \eta \tag{9}$$

where I_1 = the first stress invariant, $\sigma_1 + \sigma_2 + \sigma_3$; I_3 = the third stress invariant, $\sigma_1 \sigma_2 \sigma_3$; $p_a =$ atmospheric pressure in the same units of stresses. The value of I_1^3/I_3 equals 27 at the hydrostatic axis. The parameter η is used to describe the opening angle of the failure surface while the parameter m is employed to describe curvature of the failure surface in the meridian planes. Because of the constant mean effective stress test condition, the m will have no effects and therefore is set as zero in this study.

In Figure 9(a-c), Eq. (9) is used to fit the ϕ_p values which is shown as solid lines. The computed η values are

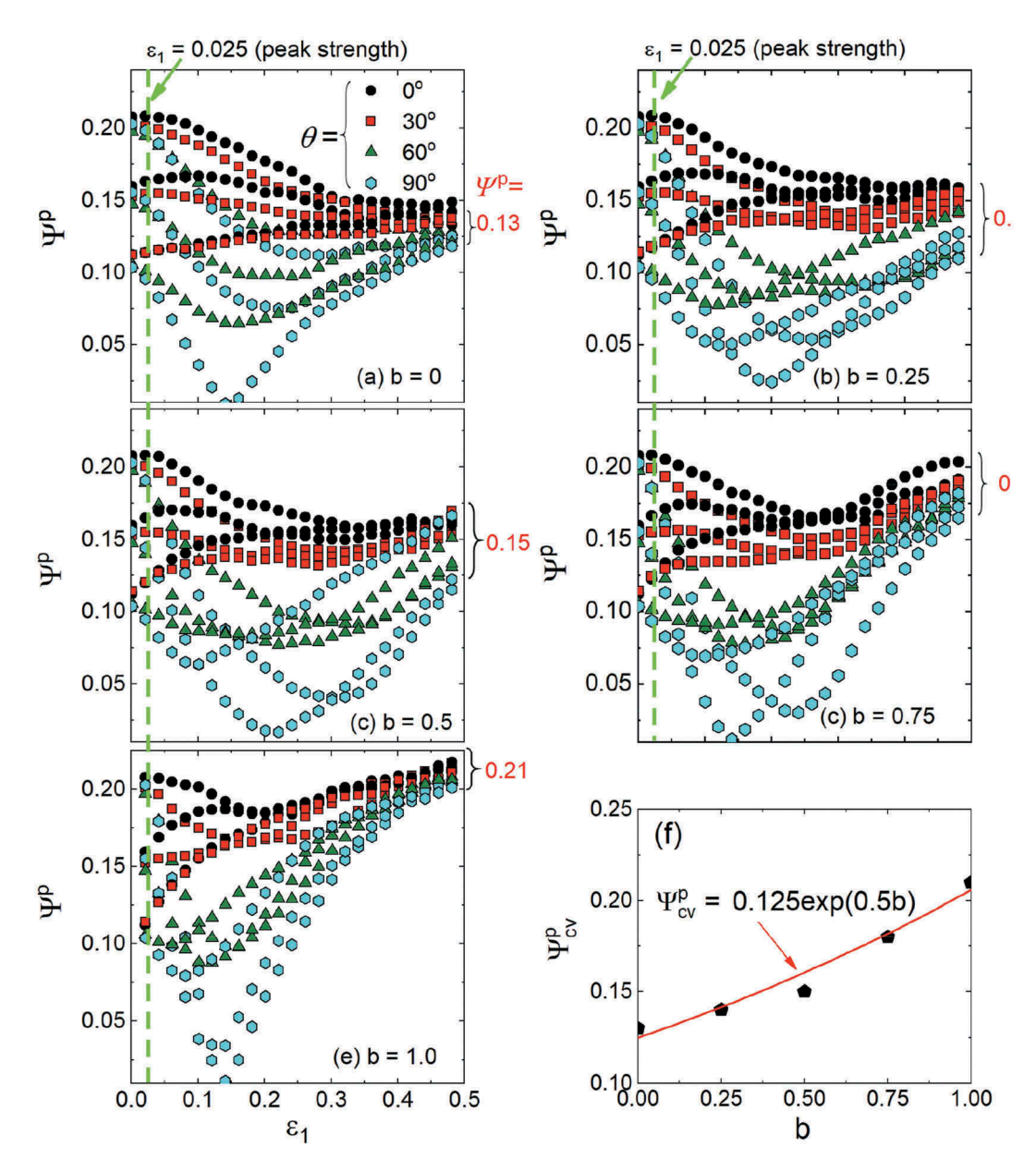


Figure 11. The evolutions of particle long axis fabric degrees with vertical strain.

shown. This study showed that even though Lade's failure criterion is an isotropic failure criterion, it can effectively dedicate the failure envelop at each inherent fabric. In Figure 9(d), the ϕ_{cv} values at different b values also follow Lade's failure envelop.

The equivalent deviatoric stress q_e can be computed using Eq. (2). Therefore, the mobilised stress ratio is defined as q_e/p '. The peak mobilised stress ratio $q_{e,p}/p$ ' is plotted against b in Figure 10(a–c). For the same b value, the $q_{e,p}/p$ ' decreases as increasing θ . However, as b increases from 0 to 1, the $q_{e,p}/p$ ' monotonically decreases displaying a different trend than ϕ_p values in Figure 9. Comparing definitions for friction angle ϕ and q_e , the q_e considers the intermediate principal stress σ_2

while ϕ does not. As b increases from 0 to 1, σ_2 increases and $q_{\rm e,p}$ decreases based on Eq. (2). The $q_{\rm e,p}/p$ values also fit Lade's failure criteria for each inherent fabric. Figure 10 (d) shows mobilised stress ratio at critical state $q_{\rm e,cv}/p$ '. For the same b value, all the $q_{\rm e,cv}/p$ ' values collapse together they are independent of fabric degree and orientation. Meanwhile for different b values, the $q_{\rm e,cv}/p$ ' values display the same trend with $q_{\rm e,p}/p$ ' values and also fit Lade's failure surface.

7. Particle long axis fabric evolution

The particle long axis fabric degree can be quantified by the octahedral fabric factor Ψ^p using Eq. (7). The

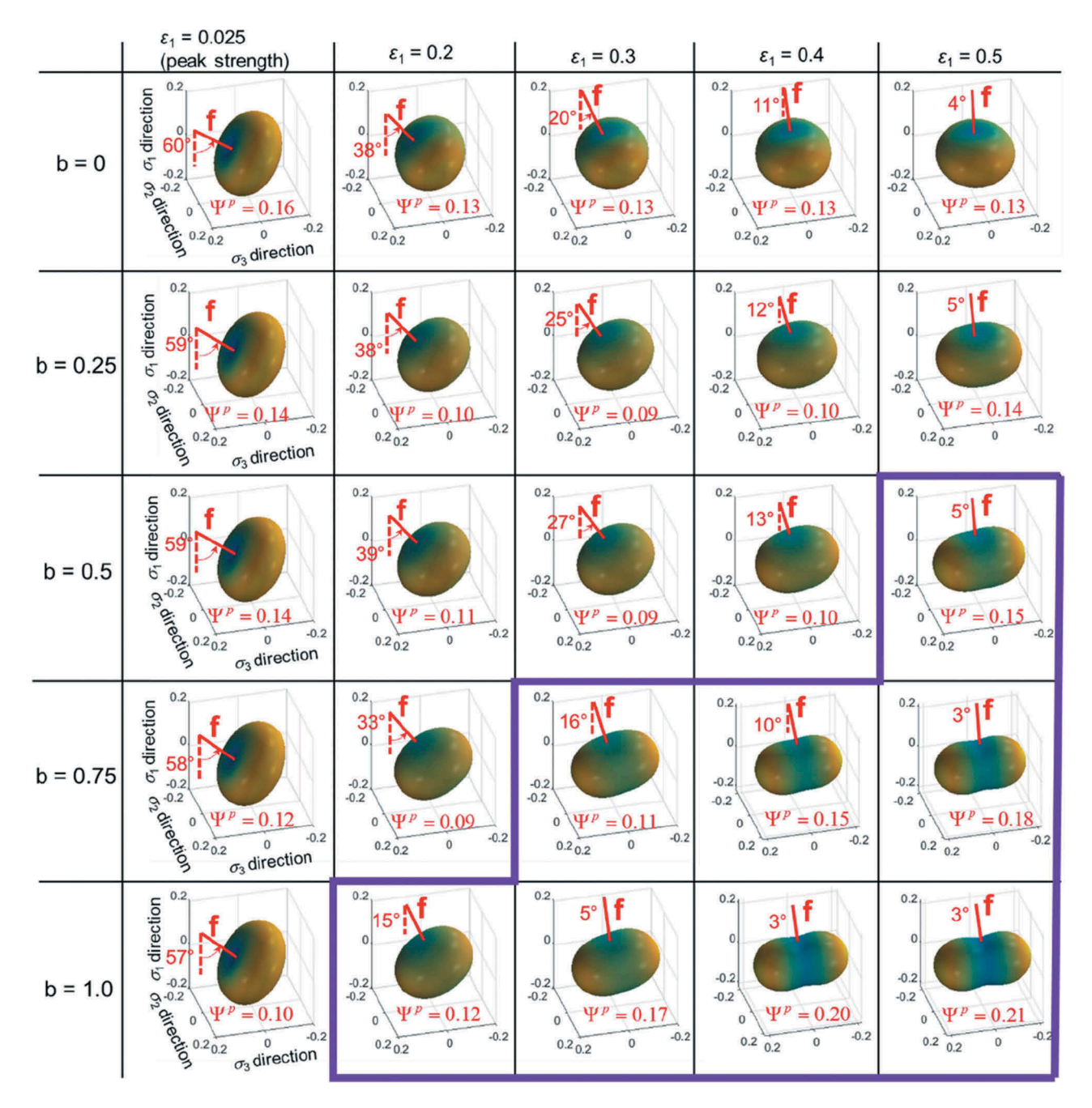


Figure 12. The typical evolution of particle long axis fabric density functions with vertical strain.

relationships between Ψ^p and ε_1 are shown in Figure 11. All the curves start from $\Psi^p = 0.20$, 0.15 or 0.11 corresponding to inherent strong, medium or weak fabrics as shown in Figure 5(a, c and e), respectively.

In Figure 11(a–e), the trends of Ψ^p curves can be divided into two groups based on initial θ values. The Ψ^p curves of $\theta=0^\circ$ and 30°continuously develop to the same octahedral fabric at the critical state (Ψ^p_{cv}) . The Ψ^p of $\theta=60^\circ$ and 90° first decrease to their minima and then increase to reach Ψ^p_{cv} , suggesting the inherent cross-anisotropic fabrics are

destroyed and after that, the particles are adjusting their orientations to form new fabric at critical state Ψ^p_{cv} .

For a specific strain condition (b value), the Ψ^p values tend to converge to a critical Ψ^p_{cv} regardless of the inherent fabric directions and fabric degrees. The Ψ^p_{cv} increases as b increases from 0 to 1 as shown in Figure 11(f) and the relationship can be approximated as

$$\Psi_{cv}^p = 0.125 \exp(0.5b)$$
 (8)

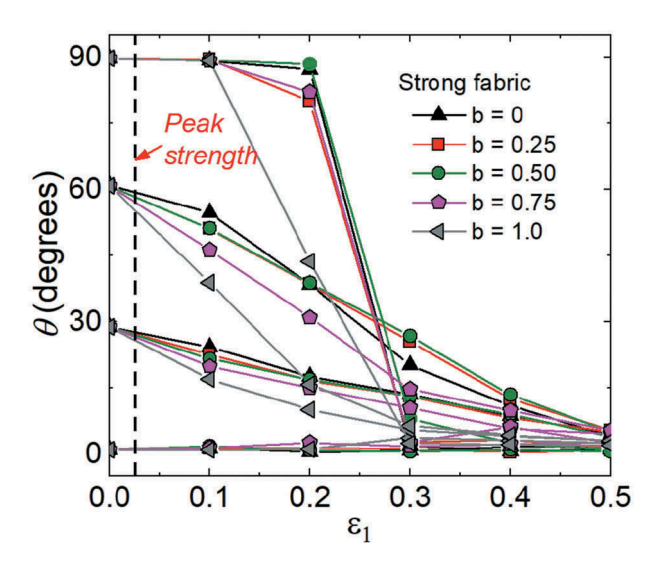


Figure 13. The typical evolutions of particle long axis fabric directions with vertical strain.

That observation is rational because high b values provide stronger constrictions at σ_2 direction and thus stronger anisotropy is developed in shear.

Figure 11 can be better visualised by plotted $E(\Omega)$ versus ε_1 . For example, the evolution of $E(\Omega)$ at $\theta=60^\circ$ is shown in Figure 12. For b=0 test, the specimen is compressed in the σ_1 direction. Therefore, the shape of $E(\Omega)$ is squeezed in σ_1 direction as ε_1 increases. For b>0 tests, the specimen is compressed at both σ_1 and σ_2 directions, so the $E(\Omega)$ is squeezed in both directions. For results highlighted in the thick polygon in Figure 12, the higher b values result in stronger anisotropic fabric developed in both σ_1 and σ_2 directions.

The evaluations of θ values with ε_1 for strong inherent fabric are shown in Figure 13. The specimens with medium fabric and weak fabric behave similarly and therefore not plotted. The θ values eventually converge to zero regardless of b and θ values. It is observed that the fabric

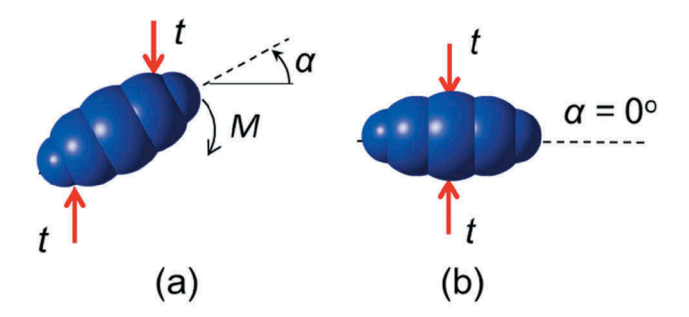


Figure 15. The particle rotation during fabric evolution.

of $\theta = 30^{\circ}$ and 60° shows a gradual transition while the fabric of $\theta = 90^{\circ}$ display a collapse at $\varepsilon_1 = 0.2 \sim 0.3$.

The evolutions of particle long axis fabric in Figure 11 to 13 can be explained by column buckling theory. In Figure 13, we observe a gradual change of fabric direction for inherent fabric direction $\theta = 0^{\circ}$, 30° , and 60° , but a sudden change for $\theta = 90^{\circ}$. This may be explained by Figure 14. The column is not stable due to the small d_s^{90} and small contact area between particles as shown in Figure 14(a). Therefore, the column collapses suddenly when reaches the buckling load. This causes the sudden transition of fabric direction for $\theta = 90^{\circ}$.

When the column collapses in Figure 14(b), orientations of particle long axes become random. Therefore, the low degrees of fabric anisotropy (or isotropic fabric) are observed at this moment when ε_1 is around 0.2. Therefore, this explains the valley of Ψ^p curves in Figure 11 when ε_1 is around 0.2.

At the critical state, the fabric direction is close to zero as shown in Figure 13, which can also be explained by buckling failure theory. The stability of particle depends on its alignment to load direction. For example, Figure 15(a) shows a particle tilting an angle of α . The vertical compression force is transmitted through the particles through a coupled forces (t) acting on top and bottom of particle. There

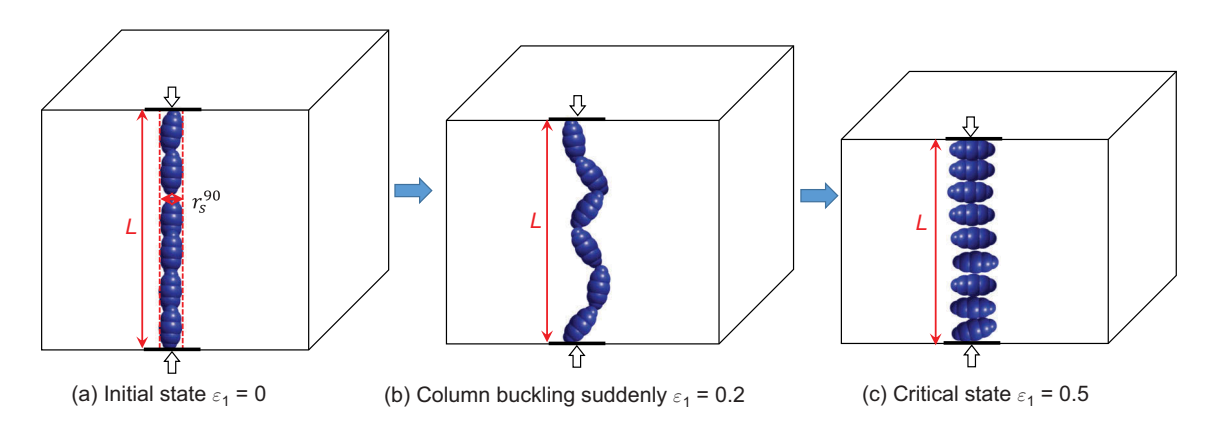


Figure 14. Column buckling theory to explain the evolution of particle long axis fabric for specimen with strong fabric and $\theta = 90^{\circ}$.

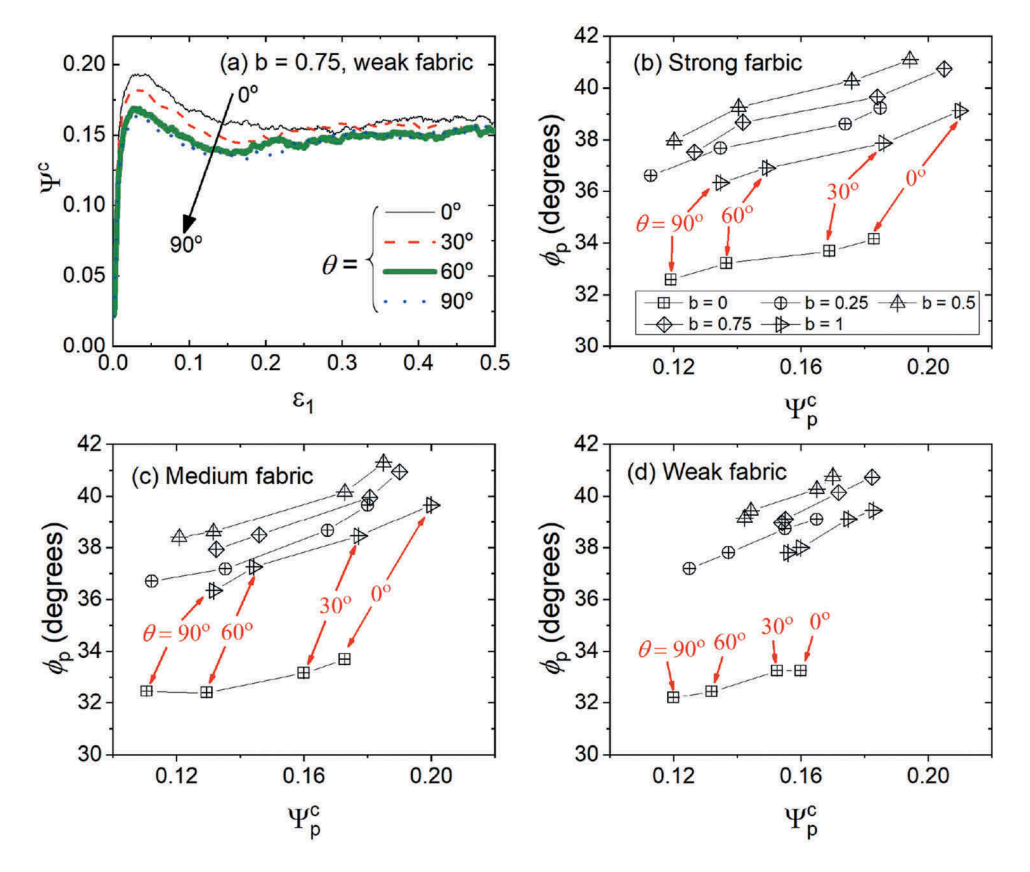


Figure 16. The evolutions of contact normal fabric degrees with vertical strain.

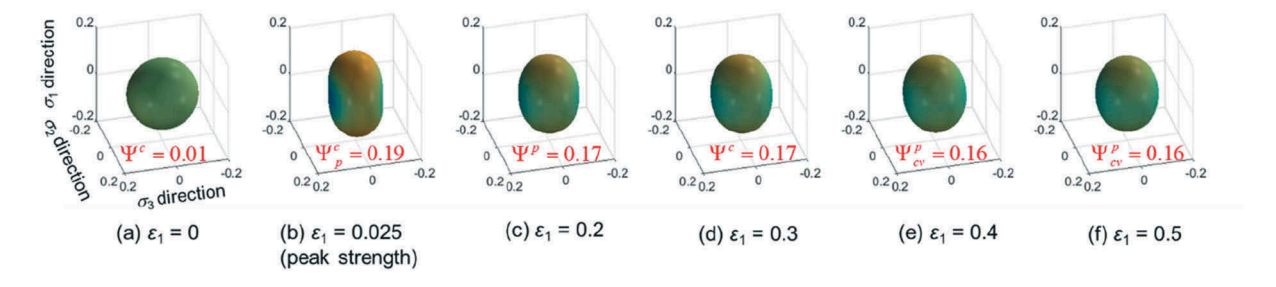


Figure 17. The typical evolutions of contact normal fabric density functions with vertical strain.

is a high tendency the coupled forces are not co-axial. Therefore, the particle will rotate due to a torque induced by a small eccentricity until reach the stable state in which α becomes zero as shown in Figure 15(b). Therefore, no matter what are the initial fabrics in the specimens, the θ values convergent to zero at critical state.

8. Contact normal fabric evolution

The contact normal fabric degree can be quantified by octahedral fabric factor Ψ^c . The evaluations of Ψ^c with axial strain ε_1 for b = 0.75 and weak fabric are shown in Figure 16(a). The initial Ψ^c values at ε_1 = 0 are close to

zero representing an isotropic fabric after consolidation. The Ψ^c curves increase to peaks around $\varepsilon_1 = 0.025$ when the $\sin(\phi)$ curves reach the peak. Then Ψ^c curves converge to the same critical state. The relationships between Ψ^c and ε_1 of other tests display similar trends as Figure 16(a), so they are not plotted.

The peak Ψ^c values (Ψ_p^c) are determined for all the simulations and plotted against ϕ_p in Figure 16(b–d). As shown, for the same b condition, both Ψ_p^c and ϕ_p are increases as θ decreases from 90° to 0° suggesting strong fabric anisotropy is generated at higher shear strength.

The density function $E(\Omega)$ for inherent fabric of θ = 0° and weak fabric under testing condition of b = 0.75 is plotted in Figure 17. After consolidation (ε_1 = 0), the E

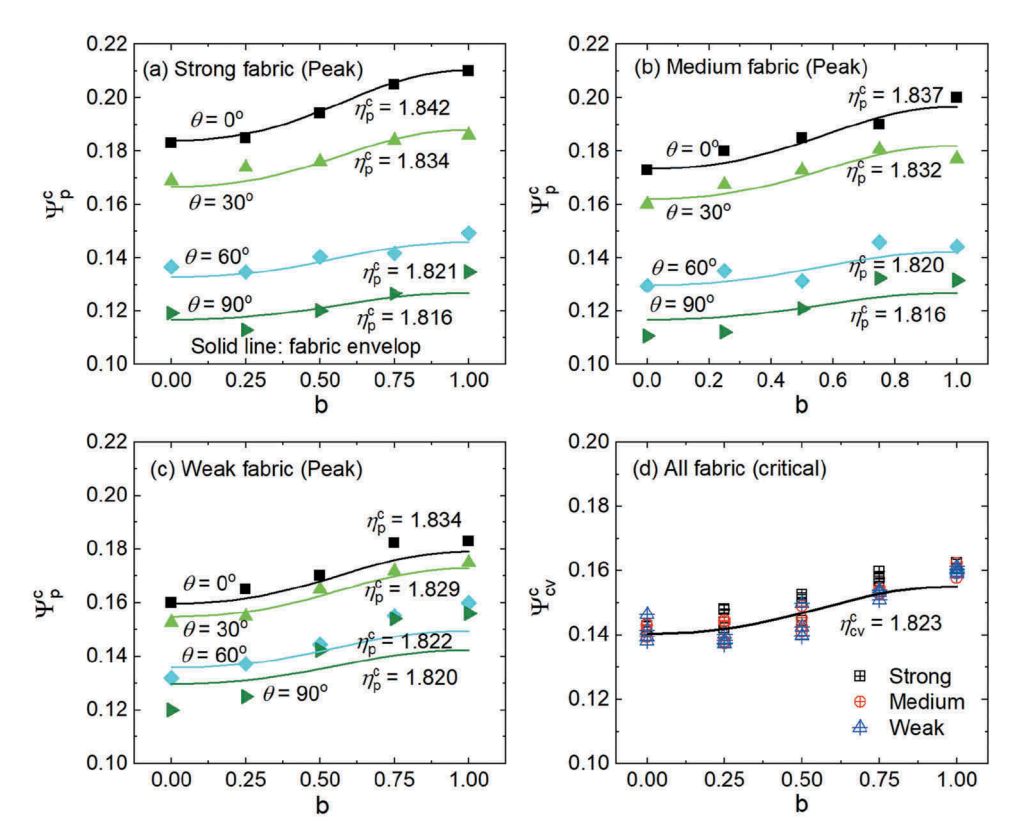


Figure 18. The relationships between peak contact normal fabric degrees (Ψ_p^c) , critical contact normal fabric degrees (Ψ_{cv}^c) , and triaxial strain conditions (b).

 (Ω) is close to a sphere representing an isotropic fabric. During the compression, the contacts between particles are mobilised to resist the vertical compression. Therefore, $E(\Omega)$ become elongated in the σ_1 direction. After peak, the Ψ^c gradually decreases to a constant value.

Comparing fabrics of particle long axes in Figure 11, 12, and 13 and contact normals in Figures 16 and 17, contact normals are immediately mobilised to resist external loads, but the particle orientations have a lagging effect. Therefore, both direction and degree of fabric formed by particle long axes have minor changes at peak shear strength when $\varepsilon_1 = 0.025$ compared with inherent fabric. However, both direction and degree of fabric formed by contact normals significantly change and correlate with evaluations of shear behaviour of soil.

The Ψ_p^c values are plotted against b values in Figure 18(a–c). The Ψ_p^c values monotonically increase as b increases. The higher b values meaning stronger constraint at the σ_2 direction and therefore stronger fabric anisotropy. If we compare Figure 18 with Figure 10, the Ψ_p^c values take an inverted trend of $q_{\rm e,p}/p^c$ values. Therefore, the inverted Lade's failure surface is defined to fit Ψ_p^c values (Thornton and Zhang 2010):

$$\frac{1}{2\Psi_2^c - 3\Psi_3^c} = \eta^c \tag{9}$$

where the Ψ_2^c and Ψ_3^c are second and third contact fabric invariants: $\Psi_2^c = \varphi_1 \varphi_2 + \varphi_1 \varphi_3 + \varphi_2 \varphi_3$ and $\Psi_3^c = \varphi_1 \varphi_2 \varphi_3$; and the η^c is a constant related to the degree of fabric anisotropy. Eq. (9) well fits the contact fabrics. The Ψ^c at strain range of $\varepsilon_1 = 0.4 \sim 0.5$ is averaged to compute the critical octahedral contact fabric factor Ψ_{cv}^c . The Ψ_{cv}^c values for the same b collapse together meaning the critical fabric is independent of initial fabric degrees and directions. The Ψ_{cv}^c values for the same b values also follow the inverted Lade's failure envelope.

9. Conclusions

This study conducts DEM simulations to explore the evaluations of fabric anisotropy of granular soils in triaxial tests and discover a fundamental understanding of anisotropic shear strength of granular soils observed in laboratory tests.

In this study, soil particles are idealised as ellipsoids to preserve the elongation distributions of real soil particles determined by analysing 90,000

particles from 18 sands. Then, virtual soil specimens are prepared at different inherent fabrics including four fabric directions of $\theta = 0^{\circ}$, 30°, 60°, and 90°. At each fabric direction, strong, medium, and weak fabrics are simulated. Therefore, 12 inherent fabrics are generated. The triaxial tests are simulated at five intermediate stress ratio values with b values of 0, 0.25, 0.5, 0.75, and 1.0. Therefore, a total of 60 DEM simulations are performed.

Simulations show that shear strength (ϕ_p) decreases as θ increases from 0° to 90°, which agrees well with the laboratory test results. The decreasing ranges $(\Delta \phi_p)$ are different depending on the inherent fabric degrees and b values. The $\Delta \phi_{\rm p}$ values for strong and medium fabrics are close and both are larger than $\Delta \phi_p$ for weak fabric. The $\Delta \phi_{\rm p}$ increases as b increase.

The mobilised shear strength evolutions correlate with the evolutions of contact normal fabrics. The fabric degree (Ψ^c) and friction angle (ϕ) reach their peak values (Ψ_p^c and ϕ_p) at the same strain level of $\varepsilon_1 = 0.025$. Then, they reduce to the critical state values (Ψ_{cv}^c and ϕ_{cv}) regardless of inherent fabrics. Larger ϕ_p values correspond to larger Ψ_p^c . Lade's failure criterion for cohensionless soils can be used to describe shear strength and contact fabric anisotropy at both peak and critical states at a certain inherent fabric.

Particle long axis fabric shows a lagging effect than contact normal fabric. When soils reach the peak shear strength at $\varepsilon_1 = 0.025$, particle long axis fabrics do not change from the inherent fabrics. Therefore, particle orientations are preserved. Based on this observation, a buckling failure theory from structural engineering is introduced to explain the anisotropic strength of granular soils and fabric evaluations. The conceptual soil columns are cut from soil specimens with different inherent fabrics. When θ increase from 0° to 90° in inherent fabrics, the widths of conceptual soil columns decrease, leading to smaller shear buckling loads, and therefore, smaller shear strengths of granular soils.

Acknowledgments

This material is based upon work supported by the U.S. National Science Foundation under Grant No. CMMI 1917332. Any opinions, findings, and conclusions or recommendations expressed in this material are those of the authors and do not necessarily reflect the views of the National Science Foundation.

Disclosure statement

The authors declare that they have no conflict of interest.

Funding

This work was supported by the Division of Civil, Mechanical and Manufacturing Innovation [1917332].

ORCID

Junxing Zheng (b) http://orcid.org/0000-0001-9428-3969 Hantao He http://orcid.org/0000-0003-2532-4952 Zhaochao Li http://orcid.org/0000-0003-0988-5792

References

Arthur, J.R.F., Chua, K.S., and Dunstan, T., 1977. Induced anisotropy in sand. Geotechnique, 27, 13-30. doi:10.1080/ 19397030902947041

Arthur, J.R.F. and Menzies, B.K., 1972. Inherent Anisotropy in a sand. Géotechnique. doi:10.1680/geot.1973.23.1.128

Arthur, J.R.F. and Phillips, A.B., 1975. Homogeneous and layered sand in triaxial compression. Géotechnique, 25, 799-815. doi:10.1680/geot.1975.25.4.799

Azami, A., Pietruszczak, S., and Guo, P., 2009. Bearing capacity of shallow foundations in transversely isotropic granular media. International Journal for Numerical and Analytical Methods in Geomechanics, 34, 771-793. doi:10.1002/nag.827

Barreto, D. and O'Sullivan, C., 2012. The influence of inter-particle friction and the intermediate stress ratio on soil response under generalised stress conditions. Granular Matter, 14, 505-521. doi:10.1007/s10035-012-0354-z

Christoffersen, J., Mehrabadi, M.M., and Nemat-Nasser, S., 1981. A micromechanical description of granular material behavior. Journal of Applied Mechanics, 48, 339-344. doi:10.1115/1.3157619

Cui, L., O'Sullivan, C., and O'Neill, S., 2007. An analysis of the triaxial apparatus using mixed a three-dimensional discrete element model. Géotechnique, 57, 831-844. doi:10.1680/geot.2007.57.10.831

Guo, N. and Zhao, J., 2013. The signature of shear-induced anisotropy in granular media. Computers and Geotechnics, 47, 1–15. doi:10.1016/j.compgeo.2012.07.002

Hryciw, R.D., Zheng, J., and Shetler, K., 2016. Particle roundness and sphericity from images of assemblies by chart estimates and computer methods. Journal of Geotechnical and Geoenvironmental Engineering, 142, 04016038. doi:10.1061/(ASCE)GT.1943-5606.0001485

Huang, X., et al., 2014. DEM analysis of the influence of the intermediate stress ratio on the critical-state behaviour of granular materials. Granular Matter, 16, 641-655. doi:10.1007/s10035-014-0520-6

Itasca Consulting Group, 2018. Particle flow code in two and dimensions, user's manual. Version, Minneapolis, MN: Itasca Consulting Group Inc.

Kanatani, K., 1984. Distribution of directional data and fabric tensors. The International Journal of Engineering Science, 22, 149-164. doi:10.1016/0020-7225(84)90090-9

Krumbein, W.C. and Sloss, L.L., 1951. Stratigraphy and sedimentation. San Francisco: W.H. Freeman and Company.

Lade, P.V., 1977. Elasto-plastic stress-strain theory for cohesionless soil with curved yield surfaces. International



- Journal of Solids and Structures, 13, 1019-1035. doi:10.1016/0020-7683(77)90073-7
- Lade, P.V., Rodriguez, N.M., and Van Dyck, E.J., 2014. Effects of principal stress directions on 3D failure conditions in cross-anisotropic sand. Journal of Geotechnical and Geoenvironmental Engineering, 140, 1-12. doi:10.1061/ (ASCE)GT.1943-5606.0001005
- Lade, P.V., Van Dyck, E.J., and Rodriguez, N.M., 2015. Shear banding in torsion shear tests on cross-anisotropic deposits of fine Nevada sand. Soils and Foundations, 54, 1081-1093. doi:10.1007/978-3-319-13506-9 13
- Lam W-K, T.F. and Tatsuoka, F., 1988. Effects of initial anisotropic fabric and intermediate stress on strength and deformation characteristics of sand. Soils and Foundations, 28, 89-106. doi:10.3208/sandf1972.28.89
- Li, Z., et al., 2019b. Collapse mechanism of the thin-walled functionally graded cylinders encased in the saturated permeable mediums. Engineering Structures, 198, 109472. doi:10.1016/j.engstruct.2019.109472
- Li, Z., et al., 2019c. Nonlinear stability analysis of thin-walled steel pipe confined in soft bilayer medium. Engineering Structures, 196, 109318. doi:10.1016/j.engstruct.2019.
- Li, Z., et al., 2019d. Nonlinear structural stability performance of pressurized thin-walled FGM arches under temperature variation field. International Journal of Non-linear Mechanics, 113, 86-102. doi:10.1016/j.ijnonlinmec.2019.
- Li, Z., et al., 2019e. Nonlinear stability and buckling analysis of composite functionally graded arches subjected to external pressure and temperature loading. Engineering Structures, 199, 1–17. doi:10.1016/j. engstruct.2019.109606
- Li, Z., Zheng, J., and Chen, Y., 2019a. Nonlinear buckling of thin-walled FGM arch encased in rigid confinement subjected to external pressure. Engineering Structures, 186, 86-95. doi:10.1016/j.engstruct.2019.02.019
- Ng, T.T., 2004. Macro- and micro-behaviors of granular materials under different sample preparation methods and stress paths. International Journal of Solids and Structures, 41, 5871-5884. doi:10.1016/j. ijsolstr.2004.05.050
- O'sullivan, C., Cui, L., and O'neill, S.C., 2008. Discrete element analysis of the response of granular materials during cyclic loading. Soils and Foundations, 48, 511-530. doi:10.3208/sandf.48.511
- Ochiai, H. and Lade, P.V., 1983. Three-dimensional behavior of sand with anisotropic fabric. Journal of Geotechnical and 109, Geoenvironmental Engineering, 1313-1328. doi:10.2208/jscej1969.1983.339_147
- Oda, M., 1972a. Initial fabric and their relations to mechanical properties of granular materials. Soils and Foundations, 12, 17-36. doi:10.3208/sandf1960.12.17
- Oda, M., 1972b. The mechanism of fabric changes during compressional deformation of sand. Soils Foundations, 12, 1-18. doi:10.1248/cpb.37.3229
- Oda, M., 1981. Anisotropic strength of cohensionless sands. Journal of Geotechnical Engineering, 107, 1219-1231. doi:10.1080/19397030902947041
- Oda, M., Kazama, H., and Konishi, J., 1998. Effects of induced anisotropy on the development of shear bands in granular

- materials. Mechanics of Materials: An International Journal, 28, 103-111. doi:10.1016/S0167-6636(97)00018-5
- Oda, M., Koishikawa, I., and Higuchi, T., 1978. Experimental study of anisotropic shear strength of sand by plane strain test. Soils and Foundations, 18, 25-38. doi:10.3208/ sandf1972.18.25
- Ouadfel, H. and Rothenburg, L., 2001. 'Stress-force-fabric' relationship for assemblies of ellipsoids. Mechanics of Materials: An International Journal, 33, 201-221. doi:10.1016/s0167-6636(00)00057-0
- Sun, Q. and Zheng, J., 2019. Two-dimensional and three-dimensional inherent fabric in cross-anisotropic granular soils. Computers and Geotechnics, 116, 103197. doi:10.1016/j.compgeo.2019.103197
- Sun, Q., Zheng, J., He, H., and Li, Z. 2019. "Particulate Material Fabric Characterization from Volumetric Images by Computational Geometry," Powder Technology, 344, 804-813. doi: 10.1016/j.powtec.2018.12.070
- Tatsuoka, F., et al., 1986b. Strength and deformation characteristics of sand in plane strain compression at extremely low pressures. Soils and Foundations, 26, 65-84. doi:10.3208/sandf1972.26.65
- Tatsuoka, F., Goto, S., and Sakamoto, M., 1986a. Effects of some factors on strength and deformation characteristics of sand at low pressures. Soils and Foundations, 26, 105-114. doi:10.1248/cpb.37.3229
- Thornton, C., 2000. Numerical simulations of deviatoric shear deformation of granular media. Géotechnique, 50, 43-53. doi:10.1680/geot.2000.50.1.43
- Thornton, C. and Zhang, L., 2010. On the evolution of stress and microstructure during general 3D deviatoric straining of granular media. Géotechnique, 60, 333-341. doi:10.1680/ geot.2010.60.5.333
- Wang, J. and Gutierrez, M., 2010. Discrete element simulations of direct shear specimen scale effects. Géotechnique, 60, 395-409. doi:10.1680/geot.2010.60.5.395
- Wong, R.K.S. and Arthur, J.R.F., 1985. Induced and inherent anisotropy in sand. Geotechnique, 35, 471-481. doi:10.1080/19397030902947041
- Yang, L.T., et al., 2016. A laboratory study of anisotropic geomaterials incorporating recent micromechanical understanding. Acta Geotechnica, 11, 1111-1129. doi:10.1007/s11440-015-0423-7
- Yimsiri, S. and Soga, K., 2010. DEM analysis of soil fabric effects on behaviour of sand. Géotechnique, 60, 483-495. doi:10.1680/geot.2010.60.6.483
- Zhao, J. and Guo, N., 2015. The interplay between anisotropy and strain localisation in granular soils: a multiscale insight. Géotechnique, 65, 642-656. doi:10.1680/geot.14.P.184
- Zheng, J. and Hryciw, R.D., 2015. Traditional soil particle sphericity, roundness and surface roughness by computational geometry. Géotechnique, 65, 494-506. doi:10.1680/ geot.14.P.192
- Zheng, J. and Hryciw, R.D., 2017. Particulate material fabric characterization by rotational haar wavelet transform. Computers and Geotechnics, 88, 46-60. doi:10.1016/j. compgeo.2017.02.021
- Zheng, J. and Hryciw, R.D., 2018. Cross-anisotropic fabric of sands by wavelet-based simulation of human cognition. Soils and Foundations, 58, 1028-1041. doi:10.1016/j.sandf. 2018.06.001